Int. J. Heat Mass Transfer. Vol. 30, No. 10, pp. 2171–2187, 1987
Printed in Great Britain

0017–9310/87 $3.00 + 0.00

A continuum model for momentum, heat and species transport in binary solid–liquid phase change systems—II. Application to solidification in a rectangular cavity

W. D. BENNON and F. P. INCROPERA
Heat Transfer Laboratory, School of Mechanical Engineering, Purdue University, West Lafayette, IN 47907, U.S.A.

(*Received* 18 *December* 1986 *and in final form* 26 *March* 1987)

Abstract—A newly developed continuum model has been used with a well-established control-volume-based, finite-difference scheme to investigate solidification of a binary, aqueous ammonium chloride solution in a rectangular cavity. Advective transport of water enriched interdendritic fluids across the permeable liquidus interface has been identified as the primary mechanism for macroscopic species redistribution. The extent of this penetration is governed by the relative strengths of solutally driven mushy region flows and thermally driven flows in the bulk liquid. Unstable and double-diffusive conditions which accompany the discharge of interdendritic fluids into the liquid core have been shown to result in localized growth rate variations, remelting, and fluctuating bulk fluid transport behavior.

1. INTRODUCTION

UNLIKE solidification of a pure substance, binary mixtures do not exhibit a distinct front separating solid and liquid phases. Instead, solid is formed as a permeable, fluid saturated, crystalline-like matrix. The structure and extent of this multiphase region, known as the mushy region, depends on numerous factors, such as the specific solidification conditions and the initial composition of the liquid.

During solidification (or melting), latent energy is released (or absorbed) at the interfaces which separate the phases within the mushy region. The distribution of this energy therefore depends on the specific structure of the multiphase region. Latent energy released during solidification is transferred by conduction in the solid phase (and by advection, if the solid phase is nonstationary), as well as by the combined effects of conduction and advection in the liquid phase. Fluid motion may be induced by external means, by both thermal and solutal buoyancy forces, and by expansion or contraction of the system due to the phase transformation. Concentration variations are primarily due to differences in the solubilities of constituents within each phase. Such differences lead to the selective rejection of constituents at microscopic phase interfaces. The rejected constituents are transported by fluid advection and, to a lesser extent, by diffusion within the phases.

Difficulties associated with accommodating nondiscrete phase change and the combined influence of diffusion and advection prohibit the development of exact solutions for binary phase change systems. Consequently, research has focused on the development of numerical procedures, which can be conveniently divided into either multiple region or continuum formulations.

Multiple region formulations have been the primary focus of published literature. Such approaches involve separation of the domain into discrete regions for which conservation equations are solved independently and coupled using appropriate interface boundary conditions. While these formulations have been most frequently applied to discrete phase change in pure substances [1–3], extensions to accommodate a multiphase region have also been reported [4–6]. Regardless of the number of regions considered, difficulties center on tracking interfaces which are generally unknown functions of space and time. Often assumptions are made regarding the geometric regularity of phase interfaces, and moving numerical meshes or coordinate mapping are employed to accommodate interface motion. While the assumption of interface regularity is generally justified for discrete phase change, experimental observations for binary systems [4, 7–9] suggest that the interface separating the liquid and multiphase regions is highly irregular. The irregularity is attributed to localized variations in growth rates and/or remelting due to the combined influences of thermal and solutal fluctuations in the bulk fluid. The need for explicit consideration of interfacial boundary conditions further complicates the application of multiple region formulations. While such internal boundary conditions are relatively simple for discrete phase change, advective components of energy, momentum and species transport across the interface between the liquid and multiphase regions significantly complicate their prescription for binary systems.

The analysis of binary phase change by continuum

NOMENCLATURE

A	aspect ratio, L/H
c	specific heat
D	mass diffusion coefficient
Da	Darcy number, K_0/L^2
f	mass fraction
f^*	dimensionless mass fraction
$\bar{f}$	total mass fraction
Fo_s	solid phase Fourier number, $\alpha_s t/L^2$
g	volume fraction or gravitational acceleration
h	enthalpy
h^*	dimensionless enthalpy, $(h-h_{sol})/(h_{liq}-h_{sol})$
h_f	heat of fusion
H	cavity height
k	thermal conductivity
k^*	thermal conductivity ratio, k_s/k_l
k_p	equilibrium partition ratio, m_{liq}/m_{sol}
K	permeability
K_0	permeability coefficient
L	cavity sidewall spacing
Le	Lewis number, α_l/D_l^α
m	slope
p	pressure
Pr	Prandtl number, ν_l/α_l
q	local heat flux
$\bar{q}$	average heat flux, $\int_0^H q\,dy/H$
q^*	local dimensionless heat flux, $qL/k_l(T_0-T_e)$
$\bar{q}^*$	average dimensionless heat flux, $\bar{q}L/k_l(T_0-T_e)$
Ra_S	solutal Rayleigh number, $g\beta_S(f_{l,e}^\alpha-f_{l,0}^\alpha)L^3/\nu_l\alpha_l$
Ra_T	thermal Rayleigh number, $g\beta_T(T_0-T_e)L^3/\nu_l\alpha_l$
S_ϕ	general source term
Sc	Schmidt number, ν_l/D_l^α
Ste_l	liquid phase Stefan number, $c_l(T_0-T_e)/h_f$
Ste_s	solid phase Stefan number, $c_s(T_0-T_e)/h_f$
t	time
t^*	dimensionless time, $Fo_s\,Ste_s$
T	temperature
T^*	dimensionless temperature
T_m	fusion temperature for $f_l^\alpha=0$
u, v	x, y direction velocity components
u^*, v^*	dimensionless velocity components, uL/α_l, vL/α_l
$\mathbf{V}$	velocity vector
x, y	Cartesian coordinates
x^*, y^*	dimensionless coordinates, x/L, y/H.

Greek symbols

α	thermal diffusivity, $k/\rho c$
β_S	solutal expansion coefficient
β_T	thermal expansion coefficient
Γ	general diffusion coefficient
θ_S	dimensionless liquid composition, $(f_l^\alpha-f_{l,e}^\alpha)/(f_{l,0}^\alpha-f_{l,e}^\alpha)$
θ_S^0	dimensionless liquid composition for $f_l^\alpha=0$
θ_T	dimensionless temperature, $(T-T_e)/(T_0-T_e)$
μ	dynamic viscosity
ν	kinematic viscosity
ρ	density
ϕ	general dependent variable
ψ	stream function.

Subscripts

c	cold boundary
e	eutectic
h	hot boundary
k	phase k
l	liquid
liq	liquidus
m	evaluated at T_m
s	solid
sol	solidus
0	initial.

Superscript

α	constituent α.

or single domain methods has received considerably less attention. Continuum formulations eliminate the need to consider separate conservation equations in each phase or region by establishing conservation equations which are universally valid. While such formulations are generally more complex than those for a single phase, they eliminate the need to explicitly consider interface motion and boundary conditions internal to the solidifying domain.

Continuum formulations have been relatively well established for discrete phase change in the absence of fluid motion. Examples include effective specific heat methods [10–12] and enthalpy based formulations [13–15]. Although continuum formulations of multiconstituent phase change have also been developed [16, 17], consideration has been restricted to conditions dominated by one-dimensional diffusion. Difficulties associated with incorporat-

ing advective components of momentum, energy and species transport have discouraged the application of continuum formulations for phase change problems involving free, forced or mixed convection phenomena.

In a companion paper [18], a continuum formulation, which integrates semi-empirical laws and microscopic descriptions of transport behavior with principles of classical mixtures theory, has been developed for binary, solid–liquid phase change. Unlike much of the continuum theory literature, a degree of generality has been relinquished in an effort to establish continuum transport equations which are free of ambiguous symbolic representation and amenable to both clear physical interpretation and solution by conventional numerical procedures. The objective of this paper is to demonstrate the capabilities of the formulation by applying it to a problem of considerable importance, namely, solidification of a binary mixture in a rectangular, impermeable cavity. Although numerical treatments of thermally driven natural convection in such cavities has been extensively considered without and with phase change [19–22], little has been done to treat the problem for thermally and compositionally driven convection without phase change [23] or with phase change [24, 25]. In addition to establishing the capabilities of the formulation, the results of this study also illustrate the rich and complex transport phenomena common to problems involving multiconstituent phase change.

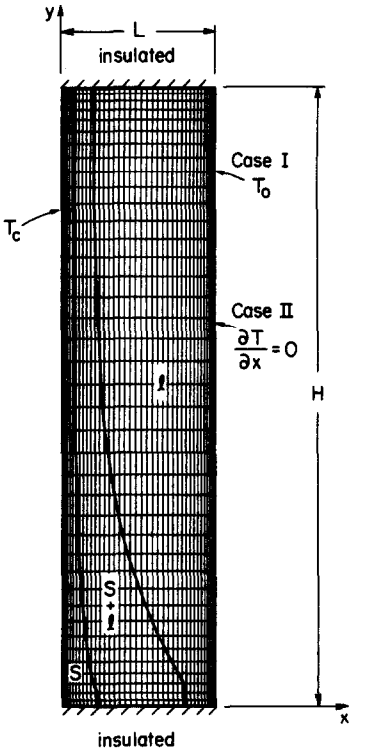

FIG. 1. Geometry and nomenclature relevant to binary solidification in a rectangular enclosure.

2. MATHEMATICAL MODEL

2.1. *Conservation equations*

Solidification is considered in a two-dimensional, rectangular impermeable cavity of dimensions $L \times H$, as shown schematically in Fig. 1. Initially, all boundaries are insulated, the cavity is charged with a superheated binary solution of composition $f_{1,0}^{\alpha}$ and temperature T_0, and the system is in equilibrium. In this study two cases are considered. For case I, solidification is induced by reducing the temperature of one vertical surface to a value T_c, which is less than the eutectic temperature T_e, while maintaining the opposing surface at the initial temperature T_0. For case II, solidification is induced by reducing the temperature of one vertical surface to T_c, while the opposing surface is insulated.

Continuum equations governing the conservation of mass, momentum, energy and species in binary, solid–liquid, phase change systems have been developed [18] and, for the system of interest, may be expressed as:

continuity

$$\frac{\partial}{\partial t}(\rho)+\nabla\cdot(\rho\mathbf{V})=0; \tag{1}$$

momentum

$$\frac{\partial}{\partial t}(\rho u)+\nabla\cdot(\rho\mathbf{V}u)=\nabla\cdot\left(\mu_1\frac{\rho}{\rho_1}\nabla u\right)-\frac{\mu_1}{K}\frac{\rho}{\rho_1}(u-u_s)-\frac{\partial p}{\partial x} \tag{2}$$

$$\frac{\partial}{\partial t}(\rho v)+\nabla\cdot(\rho\mathbf{V}v)=\nabla\cdot\left(\mu_1\frac{\rho}{\rho_1}\nabla v\right)-\frac{\mu_1}{K}\frac{\rho}{\rho_1}(v-v_s)-\frac{\partial p}{\partial y}+\rho g[\beta_T(T-T_e)+\beta_S(f_1^{\alpha}-f_{1,e}^{\alpha})]; \tag{3}$$

energy

$$\frac{\partial}{\partial t}(\rho h)+\nabla\cdot(\rho\mathbf{V}h)=\nabla\cdot\left(\frac{k}{c_s}\nabla h\right)+\nabla\left[\frac{k}{c_s}\nabla(h_s-h)\right]-\nabla\cdot[\rho(h_1-h)(\mathbf{V}-\mathbf{V}_s)]; \tag{4}$$

species

$$\frac{\partial}{\partial t}(\rho f^{\alpha})+\nabla\cdot(\rho\mathbf{V}f^{\alpha})=\nabla\cdot(\rho D\nabla f^{\alpha})+\nabla[\rho D\nabla(f_1^{\alpha}-f^{\alpha})]-\nabla\cdot[\rho(f_1^{\alpha}-f^{\alpha})(\mathbf{V}-\mathbf{V}_s)]. \tag{5}$$

The mixture density, velocity, enthalpy and species mass fraction are defined as

$$\rho=g_s\rho_s+g_l\rho_l \tag{6}$$

$$\mathbf{V} = f_s\mathbf{V}_s + f_l\mathbf{V}_l \tag{7}$$

$$h = f_s h_s + f_l h_l \tag{8}$$

$$f^\alpha = f_s f_s^\alpha + f_l f_l^\alpha \tag{9}$$

where the phase enthalpy is

$$h_k = \int_0^T c_k \, dT + h_k^0. \tag{10}$$

Similarly, the mixture thermal conductivity and mass diffusion coefficient are

$$k = g_s k_s + g_l k_l \tag{11}$$

$$D = f_l D_l^\alpha. \tag{12}$$

Assumptions invoked in the development of equations (1)–(5) include: (i) saturated mixture conditions ($g_s + g_l = 1$); (ii) laminar, constant viscosity, Newtonian flow in the liquid phase; (iii) constant phase densities except for variations in the buoyancy terms; (iv) validity of the Boussinesq approximation; (v) local thermodynamic equilibrium ($T_k = T$), and (vi) negligible species diffusion in the solid phase ($D_s^\alpha = 0$). In addition, (vii) the solid phase is assumed to be nondeforming and free of internal stress, while (viii) the multiphase region is viewed as a porous solid characterized by an isotropic permeability K. Although no general restrictions are associated with the prescription of phase specific heats and thermal conductivities, each is assumed to be constant in the present analysis. Phase enthalpies defined by equation (10) are therefore expressed as

$$h_s = c_s T \tag{13}$$

$$h_l = c_l T + [(c_s - c_l)T_e + h_f] \tag{14}$$

where it is presumed that $h_s|_{T=0} = 0$ and that $(h_l - h_s)|_{T=T_e} = h_f$.

The requirement of mixture saturation and a stress-free solid phase within the impermeable cavity necessitates the assumption that $\rho_s = \rho_l$, and hence the equality of phase volume and mass fractions ($g_k = f_k$). Without this assumption the formation of a void, for $\rho_s > \rho_l$, would violate the constraint of mixture saturation ($g_s + g_l = 1$). Similarly, for $\rho_l > \rho_s$, the constraint of a stress-free solid phase could not be enforced. The continuum conservation equations are further simplified by assuming the solid phase to be stationary ($\mathbf{V}_s = \mathbf{0}$).

Prescription of a multiphase region permeability requires consideration of growth morphology specific to the binary system under consideration. In the present analysis permeability is assumed to vary with liquid volume fraction according to the Kozeny–Carman (or Blake–Kozeny) equation [26]

$$K = K_0\left[\frac{g_l^3}{(1-g_l)^2}\right] \tag{15}$$

where K_0 is a constant which depends on the specific multiphase region morphology. In the pure solid ($g_l = 0$) and pure liquid ($g_l = 1$), equation (15) reduces to the appropriate limits, namely, $K = 0$ and ∞, respectively. Equation (15) is generally considered valid in the laminar flow regime and for liquid volume fractions less than 0.5 [27]. As such, the relationship may become suspect in regions near the liquidus interface where flow passages become dilated. In the present analysis the selection of the Kozeny–Carman equation is based on the availability of geometric data (dendrite arm spacing) for the NH_4Cl–H_2O system and its successful implementation by previous investigators [26]. Other suitably justified permeability models could, however, be easily accommodated in the present formulation.

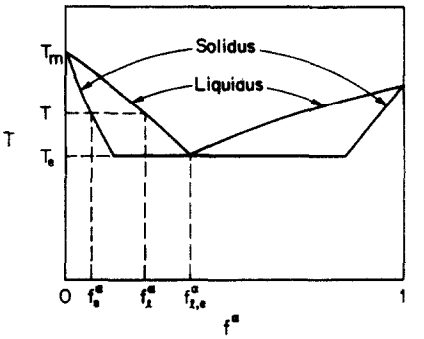

FIG. 2. Equilibrium phase diagram for a binary system.

Closure of the system of conservation equations requires supplementary relationships for phase mass fractions f_k and compositions f_k^α. With the assumption of local equilibrium, the required expressions may be obtained from the equilibrium phase diagram (Fig. 2). Neglecting solidus and liquidus line curvature, the solid mass fraction and phase compositions can be expressed as [18]

$$f_s = \frac{1}{1-k_p}\left[\frac{T - T_{liq}}{T - T_m}\right] \tag{16}$$

$$f_s^\alpha = \left[\frac{k_p}{1 + f_s(k_p - 1)}\right] f^\alpha \tag{17}$$

$$f_l^\alpha = \left[\frac{1}{1 + f_s(k_p - 1)}\right] f^\alpha \tag{18}$$

where T_{liq} is the liquidus temperature corresponding to f^α, T_m is the fusion temperature as $f^\alpha \to 0$, and the equilibrium partition ratio is the ratio of slopes for the liquidus and solidus lines ($k_p = m_{liq}/m_{sol}$). The assumption of local equilibrium does not preclude the existence of non-equilibrium conditions on a macroscopic scale. Macroscopic redistribution of species by both advective and diffusive transport is accommodated by equation (5).

2.2. *Dimensionless parameters*

The continuum conservation equations and the supplementary relationships can be solved for

velocity, enthalpy and composition fields within the solidifying domain. Difficulties arise, however, when attempts are made to represent these equations in a meaningful dimensionless form. For example, the irregular time-dependent geometry of the solid, liquid and multiphase regions and the dependence of solidus and liquidus temperatures on composition preclude the establishment of true length, temperature, and composition scales. Nevertheless, it is instructional to determine the number of possible parameter variations by casting equations (1)–(5) in dimensionless form. Omitting details of the non-dimensionalization procedure, it can be verified that the present problem is characterized by 13 dimensionless parameters which include the aspect ratio A, properties of the specific phase change system (Pr, Sc, k^*, k_p, Da), and parameters which depend on boundary and initial conditions (Ste_s, Ste_l, Ra_T, Ra_S, θ_S^0, $\theta_{T,m}$, $\theta_{T,c}$).

The physical significance of the resulting dimensionless parameters must be interpreted cautiously and should not be confused with classical single phase parameters. For example, following the onset of solidification, the sidewall spacing L is inadequate for characterizing solutal or thermal natural convection in the bulk liquid pool, and is clearly an inappropriate length scale for buoyancy driven flows in the multiphase region. In addition, the difference $(T_0 - T_e)$ is not an appropriate temperature scale for thermally induced natural convection in either the bulk liquid or multiphase regions; nor does the difference $(f_{l,e}^* - f_{l,0}^*)$ represent a meaningful composition scale for solutally driven flows. Furthermore, while both thermal and solutal Rayleigh numbers evolve from the non-dimensionalization procedure, equilibrium assumptions made in the multiphase region prohibit the independent variation of these parameters, that is $\theta_S = (\theta_S^0/\theta_{T,m})\theta_T$. Hence, only in the liquid region are thermally and solutally driven flows independent.

2.3. *Solution methodology and model validation*

Each of the continuum conservation equations have been cast in the form

$$\frac{\partial}{\partial t}(\rho\phi) + \nabla\cdot(\rho\mathbf{V}\phi) = \nabla\cdot(\Gamma\nabla\phi) + S_\phi \qquad (19)$$

where ϕ, Γ, and S_ϕ represent a general continuum-dependent variable, diffusion coefficient, and source term, respectively. Hence, any established numerical procedure for solving coupled elliptic partial differential equations can be used, with slight modifications for different S_ϕ. Since each of the continuum equations is valid throughout the entire domain, explicit consideration need not be given to boundaries between solid, multiphase and liquid regions. Hence the need for moving numerical grids and/or coordinate mapping is eliminated, as is the need for prescribing complex interfacial boundary conditions between regions internal to the domain and for making the quasi-steady approximation typically used in multiple region solutions. Explicit consideration need only be given to boundary conditions applied to external domain surfaces. Furthermore, the continuum formulation is well suited for accommodating the continuous constitutive transformation from the solid to liquid state, as well as the absorption or liberation of latent energy over a finite temperature range.

An elliptic control-volume-based finite-difference scheme [28] has been used to solve the continuum equations. Results were obtained using a slightly biased 42×42 grid, as shown in Fig. 1. Supplementary numerical calculations suggested, however, that the results are not entirely grid independent. Although calculations performed on a 52×52 grid revealed that global parameters such as average heat extraction from the chilled surface $\bar{q}_c$ and total solid $\bar{f}_s$ were within 10% of results for the 42×42 grid, heat transfer rates at the opposing vertical surface $\bar{q}_h$ (for case I) were more strongly influenced by grid size.

Differences in $\bar{q}_h$ are attributed to differences in the prediction of interface irregularities at the boundary separating the liquid and multiphase regions. Just following the onset of solidification, when growth rates are rapid, irregularities in the liquidus were not predicted for either the 42×42 or 52×52 grids, results for $\bar{q}_h$ were smooth and regular, and quantitative agreement was good. As growth rates declined, thermal and solutal variations in the bulk liquid initiated the formation of local irregularities in the liquidus, which significantly influenced liquid velocity, temperature and composition fields, and hence the predictions of $\bar{q}_h$. For times following the formation of these interface irregularities, transient fluctuations in $\bar{q}_h$ were observed for both the 42×42 and 52×52 grids, and, since the 42×42 grid could not precisely reproduce local irregularities predicted using the 52×52 grid, quantitative differences were observed. Qualitatively, however, results obtained using the 42×42 grid capture all of the physical features predicted by the finer 52×52 grid. Hence, the significant additional computational costs associated with achieving quantitative grid independence could not be justified.

Satisfactory time step independence was achieved by using $\Delta t = 3$ s ($\Delta t^* = 2.97 \times 10^{-4}$) throughout the case I simulation. For case II, this time step was doubled when growth rates ($\partial \bar{f}_s/\partial t$) fell below 1.8×10^{-4} s^{-1}. Iteration within each time step was employed to accommodate the highly non-linear and coupled nature of the equations. The number of iterations required for convergence varied from time step to time step, but was generally highest for times just following the onset of solidification. Iterations were terminated when changes in the average heat extraction from the chilled wall $\bar{q}_c$, changes in total mass fraction solid $\bar{f}_s$, and changes in minimum and maximum compositions were each below 0.001%. Computations were carried out on a Cyber 205 super computer and, for the 42×42 grid, required approximately 200–400 CPU seconds for each 30 s of real time simulation. The total

CPU time required to complete the case I and II calculations was 3.8 and 8.9 h, respectively.

The continuum formulation and numerical solution procedures have been successfully verified through comparisons with existing one-dimensional exact solutions (Neumann problems), as well as with reported two-dimensional numerical results [15] for the limiting case of discrete phase change of a pure substance without advection. For diffusion-dominated situations, the continuum energy equation (4) is identical to classical enthalpy based models, except that, for numerical convenience, the Fourier diffusion flux has been separated into two terms. This decomposition eliminates temperature as an explicit-dependent variable and hence facilitates the use of well-established numerical procedures for dealing with elliptic partial differential equations.

The ability of the formulation to accommodate buoyancy driven flows has been verified through comparisons with existing benchmark solutions [29] for single-phase, thermally induced natural convection in a square cavity with differentially heated vertical sidewalls and insulated horizontal boundaries. For a 42×42 grid, a Prandtl number of 0.71, and thermal Rayleigh numbers up to 10^6, average Nusselt numbers agreed to within 2%. Hence, the numerical procedures accurately accommodate advective components of momentum and energy transfer. Also, since the calculations were performed using continuum conservation equations developed for multiphase problems, the agreement verifies that the continuum equations transform, as they must, to well-established single phase conservation equations.

Comparison of the predictions of this study with quantitative experimental results is precluded by the paucity of such data for solidification in binary systems and/or by the absence of reliable thermophysical properties. However, important physical insights have been derived from visualization studies performed with transparent mixtures, and attempts have been made to insure that the predictions of this study are consistent with the experimental observations.

3. RESULTS

Calculations were performed for an aqueous solution of ammonium chloride (NH_4Cl–H_2O). This system was chosen because flow visualization results have been reported [4, 7–9], thermophysical property data are relatively well established [4, 26, 30, 31], and the system exhibits dendritic growth which is analogous to an important class of metal alloys. Since the problem of interest depends on eight dimensionless parameters, a comprehensive parametric investigation was deemed impractical and, in fact, unnecessary to demonstrate the capabilities of the continuum model. Calculations were therefore performed for a fixed, but representative, set of initial ($T_0 = 311$ K, $f_{l,0}^{\alpha} = 0.700$) and cold wall ($T_c = 223$ K) conditions, with the opposite wall maintained at $T_h = T_0$ (case I) or adiabatic (case II). The corresponding thermophysical properties and dimensionless parameters are listed in Table 1.

Table 1. Thermophysical properties of NH_4Cl–H_2O ($\alpha = H_2O$)

	Solid	Liquid
Specific heat (J kg^{-1} K^{-1})	1870	3249
Thermal conductivity (W m^{-1} K^{-1})	0.393	0.468
Density (kg m^{-3})	1078	1078
Diffusion coefficient (m^2 s^{-1})	—	4.8×10^{-9}
Viscosity (kg m^{-1} s^{-1})	—	1.3×10^{-3}
Latent heat of fusion, h_f (J kg^{-1})	3.138×10^5	
Permeability coefficient, K_0 (m^2)	5.56×10^{-11}	
Thermal expansion coefficient, β_T (K^{-1})	3.832×10^{-4}	
Solutal expansion coefficient, β_S	0.257	
Eutectic temperature, T_e (K)	257.75	
Eutectic composition, $f_{l,e}^{\alpha}$	0.803	
NH_4Cl melting point, T_m (K)	633.59	
Equilibrium partition ratio, k_p	0.30	
Dimensionless parameters		
Aspect ratio, A ($H = 0.1$ m)	0.25	
Prandtl number, Pr	9.025	
Schmidt number, Sc	251.3	
Thermal conductivity ratio, k^*	0.840	
Darcy number, Da	8.896×10^{-8}	
Stefan numbers, Ste_s/Ste_l	0.317/0.551	
Rayleigh numbers, Ra_T/Ra_S	$1.938 \times 10^7/2.514 \times 10^7$	
θ_S^0	7.796	
$\theta_{T,m}$	7.064	
$\theta_{T,c}$	−0.650	

3.1. *Case I: differentially heated sidewalls*

Figures 3–7 illustrate velocity, streamline, isotherm and liquid isocomposition distributions for case I at dimensionless times of $t^* = 0.009$, 0.018, 0.036, 0.071, and 0.142, respectively. Velocity vectors shown in each figure are based on the continuum velocity components u and v which, for $\mathbf{V}_s = \mathbf{0}$, can be alternately expressed as $f_l u_l$ and $f_l v_l$, respectively. For the sake of clarity, solidus and liquidus contours are shown only on the velocity plots and represent lines corresponding to $h^* = 0$ and 1, respectively, where $h^* = (h - h_{sol})/(h_{liq} - h_{sol})$.

Due to the existence of counter rotating cells, stream functions in the bulk liquid and mushy regions are of opposite signs. Maximum streamfunction values are therefore designated by $\psi_{max,l}$ and $|\psi_{max,s+l}|$ in the bulk liquid and mushy regions, respectively, and can be used to infer the relative strengths of recirculating flows in these regions. In each of Figs. 3(b)–7(b), bulk liquid streamlines are plotted in increments of $\psi_{max,l}/10$ and mushy region streamlines in increments of $|\psi_{max,s+l}|/4$.

Isotherms depicted in Figs. 3(c)–7(c) represent lines of constant $T^* = (T - T_c)/(T_0 - T_c)$, with the chilled and heated vertical boundaries represented by $T^* = 0$ and 1, respectively. Liquid isocomposition lines shown in Figs. 3(d)–7(d) represent lines of constant

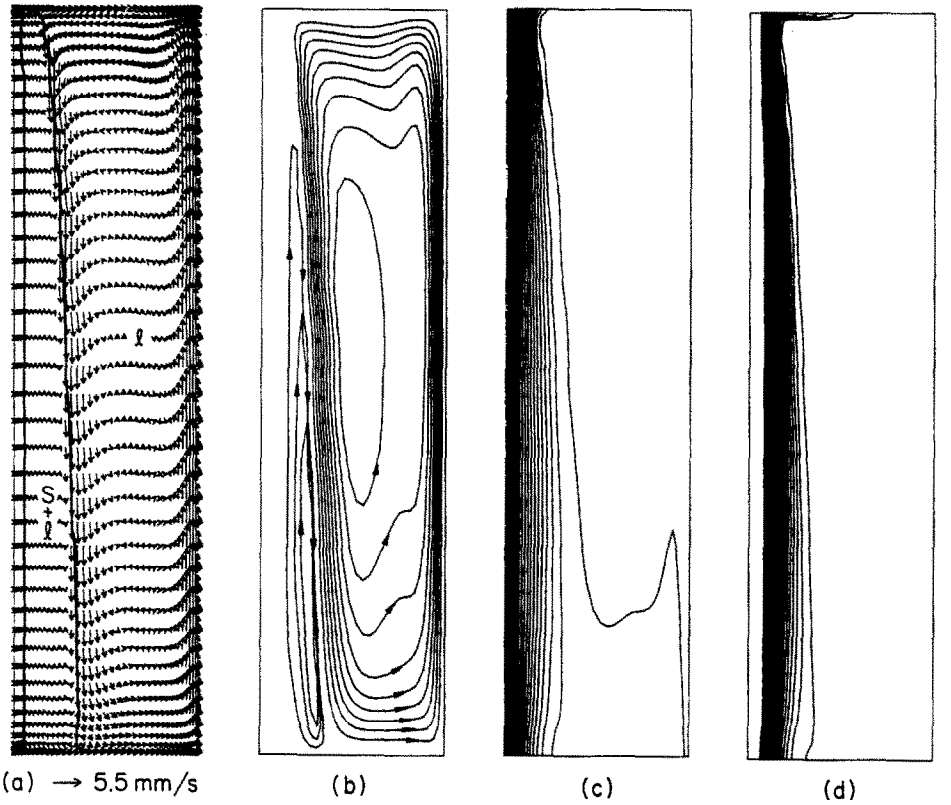

FIG. 3. Solidification behavior at $t^* = 0.009$ for case I: (a) velocity vectors, (b) streamlines ($\psi_{\max,l} = 1.53 \times 10^{-2}$, $|\psi_{\max,s+l}| = 6.05 \times 10^{-4}$), (c) isotherms, (d) liquid isocomposition lines ($f^{\alpha}_{l,\min} = 0.700$).

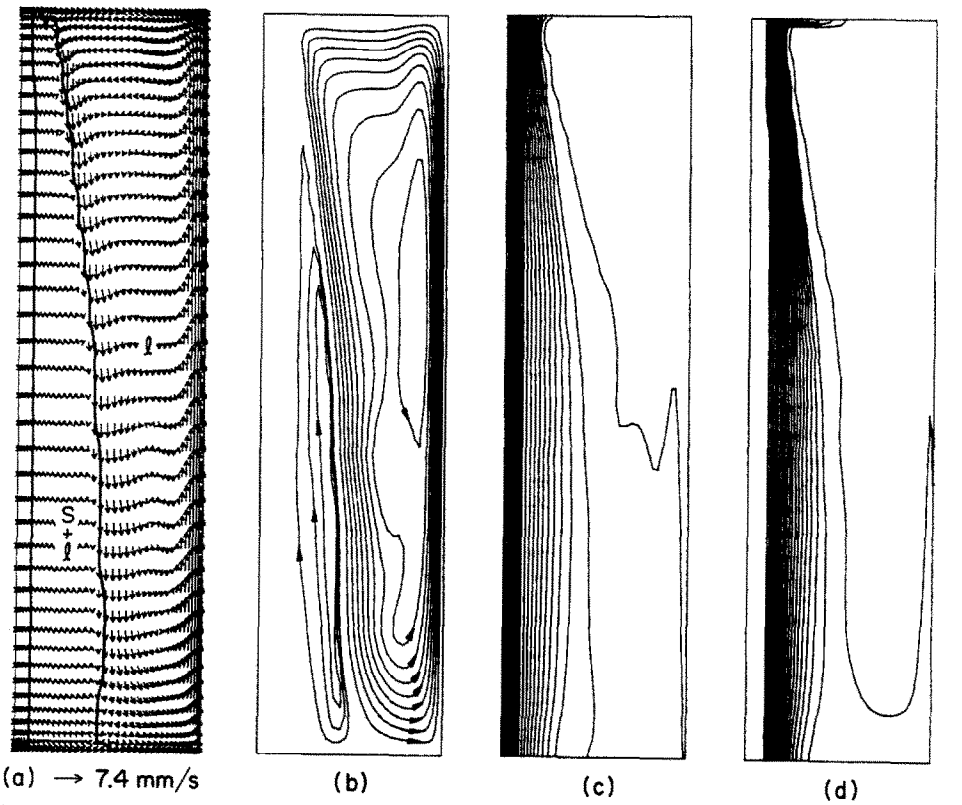

FIG. 4. Solidification behavior at $t^* = 0.018$ for case I: (a) velocity vectors, (b) streamlines ($\psi_{\max,l} = 1.70 \times 10^{-2}$, $|\psi_{\max,s+l}| = 8.26 \times 10^{-4}$), (c) isotherms, (d) liquid isocomposition lines ($f^{\alpha}_{l,\min} = 0.701$).

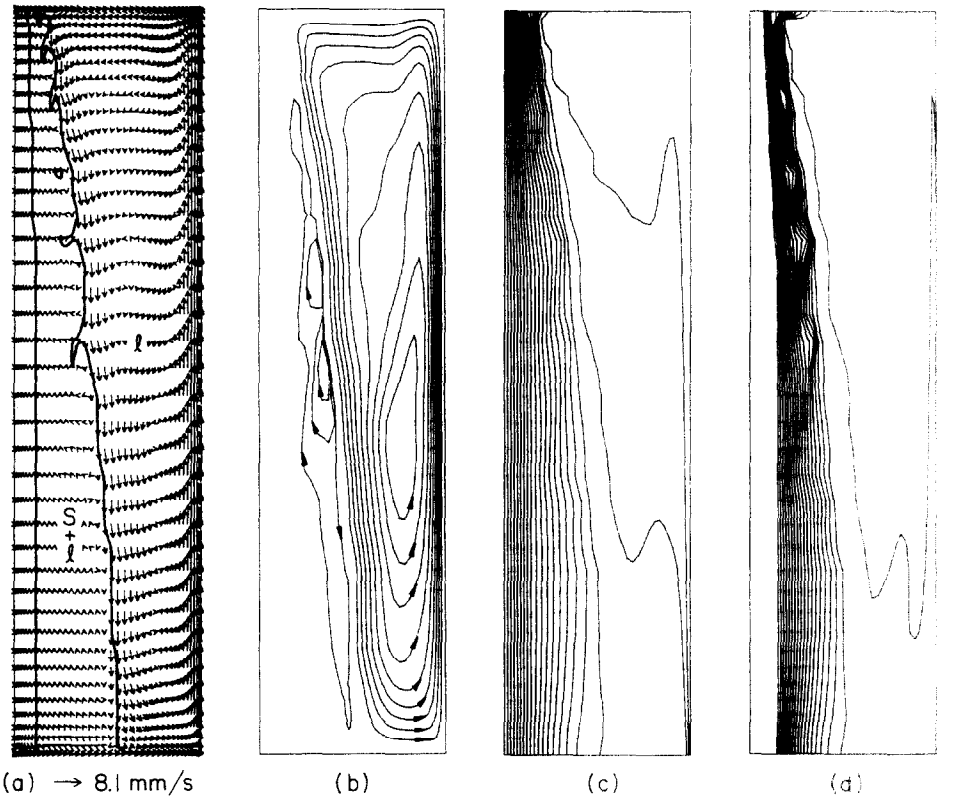

FIG. 5. Solidification behavior at $t^* = 0.036$ for case 1: (a) velocity vectors, (b) streamlines ($\psi_{max,l} = 2.04 \times 10^{-2}$, $|\psi_{max,s+l}| = 6.74 \times 10^{-4}$), (c) isotherms, (d) liquid isocomposition lines ($f^*_{l,min} = 0.709$).

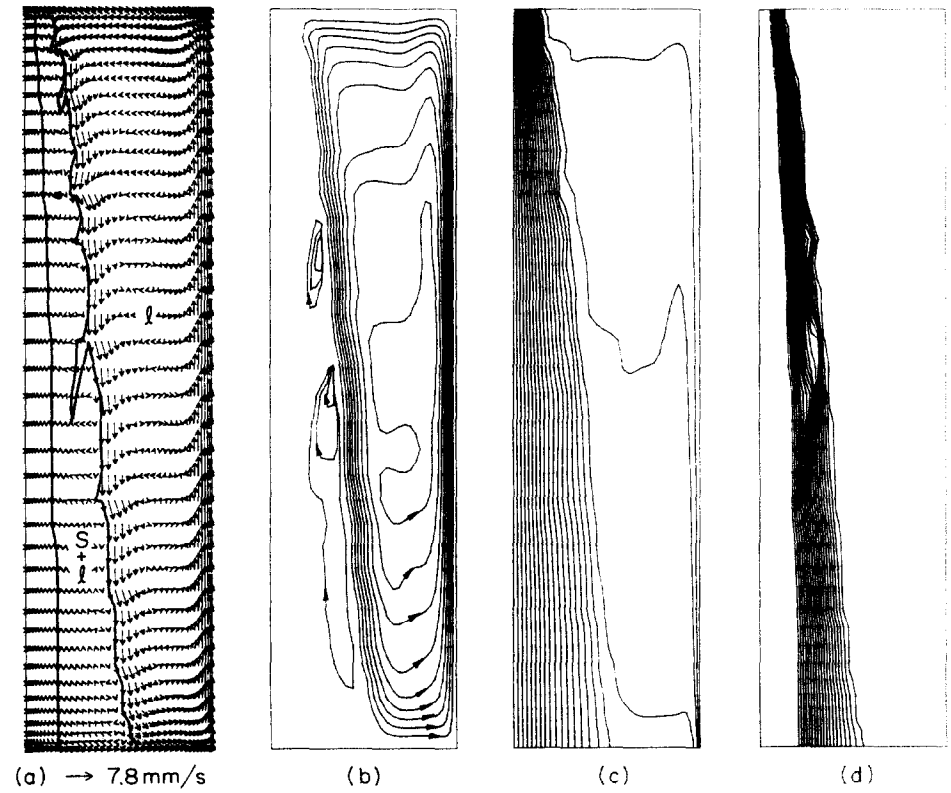

FIG. 6. Solidification behavior at $t^* = 0.071$ for case 1: (a) velocity vectors, (b) streamlines ($\psi_{max,l} = 1.71 \times 10^{-2}$, $|\psi_{max,s+l}| = 1.97 \times 10^{-4}$), (c) isotherms, (d) liquid isocomposition lines ($f^*_{l,min} = 0.719$).

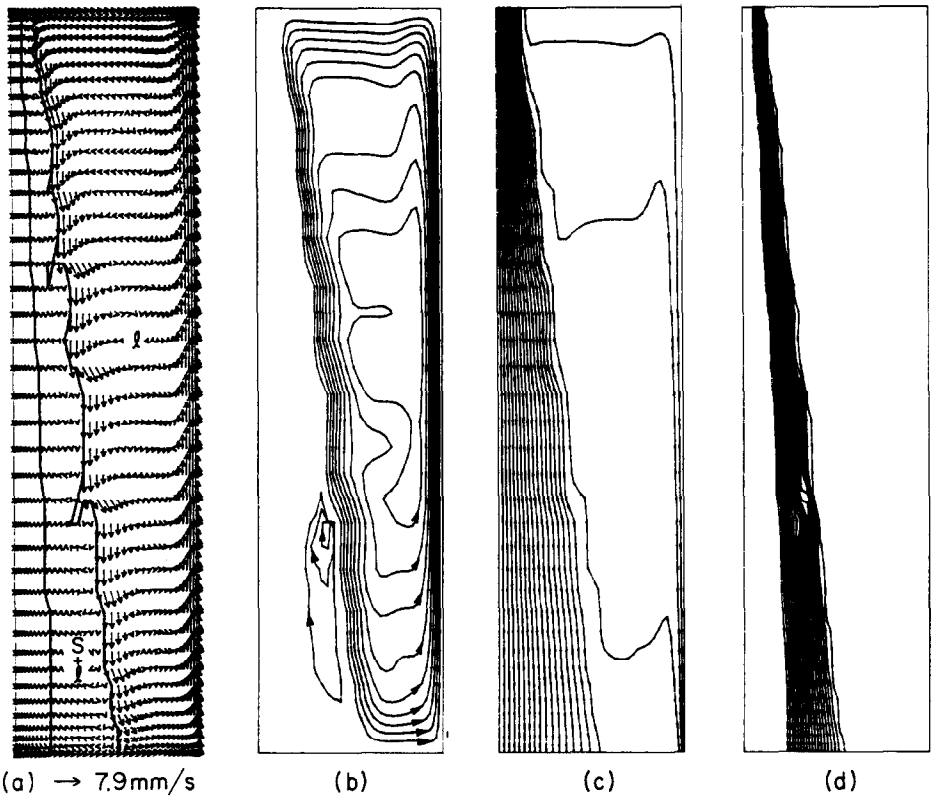

FIG. 7. Solidification behavior at $t^* = 0.142$ for case I: (a) velocity vectors, (b) streamlines ($\psi_{max,l} = 1.71 \times 10^{-2}$, $|\psi_{max,s+l}| = 6.19 \times 10^{-5}$), (c) isotherms, (d) liquid isocomposition lines ($f^{\alpha}_{l,min} = 0.725$).

$f_l^* = (f_l^{\alpha} - f_{l,min}^{\alpha})/(f_{l,e}^{\alpha} - f_{l,min}^{\alpha})$, with species α corresponding to H_2O and the solidus line representing the maximum liquid composition $f_l^* = 1$. Both T^* and f_l^* are plotted in increments of 1/20.

Figure 3 illustrates conditions at $t^* = 0.009$ ($t =$ 90 s). Solidification is initially characterized by a rapid propagation of solidus and liquidus fronts, which remain nearly planar and free of irregularities. The isotherms (Fig. 3(c)) indicate that temperature gradients are concentrated in the solid, and to a lesser extent mushy, region and that energy transport is approximately unidirectional and conduction dominated. Deviations from linearity in the outer extent of the mushy region and in the liquid core result from advective flows of interdendritic and bulk fluids, respectively.

Liquid composition profiles (Fig. 3(d)) show that gradients are confined primarily to the mushy region, with the bulk fluid core remaining at approximately the initial composition. Hence, the recirculating flow in the bulk liquid is initially due to thermal buoyancy. However, while hydrodynamic and thermal boundary layer development on the heated vertical surface is analogous to that occurring in classical single phase cavity problems [29], downflow of bulk fluid along the chilled liquidus cannot be viewed in the same manner. In particular, the permeable liquidus interface is not a *no-slip* boundary and, as illustrated in Fig. 3(a), can accommodate advective transport.

Within the mushy region, solutally driven flows of lighter, water rich interdendritic fluids establish a recirculation pattern in which upflow occurs near the solidus and downflow occurs just inside the liquidus. Upflows established nearest the solidus have the largest (nearly eutectic) concentration of water and are able to ascend further than flows established closer to the liquidus. Although most of the interdendritic fluid is confined to the recirculating flow within the mushy region, the momentum of upflow along the solidus is sufficient to facilitate penetration of the liquidus by a portion of this fluid. As shown in Fig. 3(d), this penetration creates a water rich fluid layer at the top of the cavity. The extent to which this layer can penetrate horizontally along the cavity top is limited by the strength of the opposing, thermally driven flow in the bulk fluid. A liquidus temperature depression accompanies the water enrichment of bulk fluids at the top of the cavity. Together with the incidence of warm fluid driven by the heated vertical boundary, this depression causes a reduction in local growth rates and a *thinning* of the solidus and liquidus fronts near the cavity top.

It is important to recognize that, while thermal and solutal influences are independent in the bulk liquid

core, they are not independent, by virtue of equilibrium assumptions, within the mushy region. That is, although buoyancy contributions appearing in the y-momentum equation can be written as $[Ra_T\theta_T - Ra_S\theta_S]$, within the mushy region the contributions can be expressed exclusively in terms of the temperature θ_T, $[(Ra_T-(\theta_S^0/\theta_{T,m})Ra_S)\theta_T]$. For the conditions of this study (Table 1), this result implies that, under the influence of gravity alone, buoyancy driven upflow would persist throughout the mushy region. Hence the downflow which is predicted to exist near the liquidus of the mushy region (Fig. 3(a)) must be due to the penetration of bulk liquid across the liquidus interface and to the attendant shear forces imparted to neighboring interdendritic fluids. The penetration of interdendritic fluids into the liquid core at the cavity top suggests that, in this region, advective flows outside the liquidus are of insufficient strength to overcome buoyancy driven upflows within the mushy region.

The flows within the bulk liquid and mushy regions which are suggested by Figs. 3(a) and (b) are consistent with qualitative experimental observations made by previous investigators. Using Schlieren photography and injection of dye tracers, recirculating flows characterized by downflow along the liquidus and upflow along an opposing heated vertical boundary have been observed within the bulk fluid of an ammonium chloride–water casting [4]. In addition, Schlieren photographs [4] confirm the existence of a water rich fluid layer in the bulk fluid at the top of the cavity.

Although they are more difficult to perform, observations of recirculating flows within the mushy region have been made by introducing crystals of potassium permanganate into NH_4Cl–H_2O castings [8, 9, 26]. In these studies, flows of rich interdendritic fluids within the mushy region (Fig. 3(b)) have been identified as the primary cause of channel-type 'A' and 'V' segregation observed in large commercially cast metallic ingots.

Figure 4 ($t = 180$ s) indicates significant deviations from planar, conduction dominated phase change. A solutally driven recirculating cell persists within the mushy region (Fig. 4(b)), and as shown in Fig. 4(d), there is slight erosion of the water rich layer at the cavity top. Erosion of this layer, as well as outflow of interdendritic fluids from the mushy region, leads to a double-diffusive downflow of water rich fluid along the liquidus, with subsequent upflow along the heated vertical boundary. Conditions are double-diffusive in the sense that temperature and composition gradients make opposing contributions to the vertical density distribution and the diffusivities of energy and species transport are different ($Le \neq 1$). While thermal buoyancy effects dominate and downflow persists along the liquidus, the nearly uniform velocity profiles in this region (Fig. 4(a)) and the reduction of bulk fluid penetration into the mushy zone provide a clear indication of the increased significance of opposing solutal buoyancy forces. Following deflection of the downflow by the bottom wall, positive thermal and solutal buoyancy effects combine to induce a strong upflow along the heated wall. When the heated, water enriched fluid returns to the liquidus front, it reduces growth rates and also contributes to localized remelting in a small portion of the mushy region at the cavity top.

Localized remelting and growth rate variations initiate the formation of irregularities in the liquidus front, which are clearly revealed in Fig. 4(a). Once established, interface distortions contribute to fluctuations (i.e. irregular variations with time) in velocity, temperature and composition fields within the bulk fluid. Distortions in the bulk liquid streamlines (Fig. 4(b)) and bulk liquid isotherms (Fig. 4(c)), particularly near the liquidus interface, are attributed to the existence of opposing thermal and solutal buoyancy forces, as well as to the presence of interface irregularities.

Solidification phenomena at $t = 360$ s are illustrated in Fig. 5. Local variations in the growth rate of the liquidus and macroscopic remelting resulting from thermal and solutal fluctuations in the bulk fluid manifest themselves in the establishment of a highly irregular liquidus front morphology (Fig. 5(a)), as well as the formation of liquid pockets within the mushy zone. While counterclockwise recirculation persists in the bulk fluid, the irregular liquidus front morphology, combined with the competing influences of thermal and solutal buoyancy forces, significantly distorts the bulk fluid velocity field (Fig. 5(a)) and streamlines (Fig. 5(b)).

The existence of a highly irregular liquidus interface has been experimentally observed for NH_4Cl–H_2O systems [4, 7, 8]. To the authors' knowledge, however, the present results represent the first numerical predictions of such interface behavior. Although the precise size and location of localized interface irregularities were found to be grid dependent, their appearance was not. Furthermore, such irregularities can be attributed to plausible physical mechanisms. While the present continuum formulation easily accommodates the formation of irregularities on *internal* boundaries, conventional multiple region formulations, which rely on the ability to track interface motion, would be difficult (if not impossible) to implement for phase change systems which exhibit this interface behavior.

Liquid composition profiles (Fig. 5(d)) reveal continued erosion of the water rich fluid layer at the cavity top and further development of the water rich fluid layer which descends along the liquidus front and ascends along the heated vertical surface. Distortions in the isocomposition lines which appear in the top half of the mushy region are coincidental with the liquidus front irregularities and correspond to the existence of confined liquid pockets.

Streamlines corresponding to solutally driven flow in the mushy region are no longer concentric, with

secondary cells forming near the liquidus front at locations near and below large irregularities in the front (Fig. 5(b)). Formation of these secondary cells is attributed primarily to shear forces which result from penetration of bulk fluids into the mushy region near the interface irregularities.

Temperature and liquid composition fields in the bulk fluid illustrated on both Figs. 4 and 5 are conducive to the formation of salt fingers [32], with warm salty fluid overlying cold salt-deficient fluid. The formation of these fingers is, however, inhibited by the strong counterclockwise bulk fluid recirculation.

After 720 s, solidification rates have slowed considerably at both the solidus and liquidus fronts, and liquidus front irregularities continue to distort the velocity field and associated streamlines within the bulk liquid (Figs. 6(a) and (b)). Moreover, as shown in Fig. 6(d), the water rich fluid layer at the top of the cavity has been totally eroded by the recirculating flow in the liquid core, and the bulk liquid attains a well mixed, water enriched state. The absence of composition gradients within the bulk fluid indicates that, as for $t^* = 0.009$, bulk liquid recirculation is again driven almost exclusively by thermal buoyancy forces. While significantly weakened, solutally driven flows persist within the mushy zone (Fig. 6(b)). The reduction of mushy region permeability which accompanies slower growth rates, however, limits the vertical penetration of these water rich interdendritic flows. Mushy region recirculation is again concentrated in regions near the liquidus front and below macroscopic interface irregularities.

Figure 7 illustrates conditions after 1440 s, and is representative of a quasi-steady condition ($\partial \bar{f}_s/\partial t \lesssim 10^{-5}$ s^{-1}). The bulk fluid, while enriched in water, remains well mixed and free of significant composition gradients (Fig. 7(d)). Hence, recirculation in the bulk fluid, while distorted by the persistence of liquidus front irregularities, remains driven by thermal buoyancy forces. Due to the decline in permeabilities, solutally driven recirculation within the mushy region is weak and confined to the cavity bottom.

Figure 8 depicts the transient behavior of average dimensionless hot ($\bar{q}_h^*$) and cold ($\bar{q}_c^*$) wall heat fluxes, as well as the total mass fraction of solid ($\bar{f}_s$). Only the magnitudes of the average heat fluxes are presented, with $\bar{q}_c^*$ and $\bar{q}_h^*$ representing energy extraction and addition, respectively.

Heat extraction from the chilled surface ($\bar{q}_c^*$) declines rapidly during the initial stages of solidification, when growth rates are large, and quickly approaches a quasi-steady value. As the isotherms of Figs. 3(c)–7(c) suggest, temperature distributions within the solid layer are nearly linear throughout the phase change process. This observation, combined with the fact that the solidus represents an isotherm corresponding to the eutectic temperature T_e, suggests that $\bar{q}_c^*$ is proportional to the solid layer thickness. As such, any irregularity in the variation of $\bar{q}_c^*$ with time

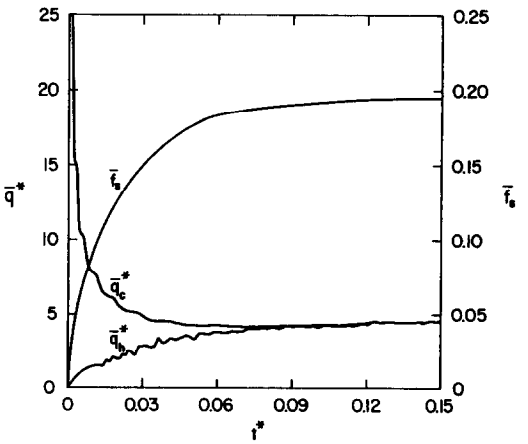

FIG. 8. Transient variations of average dimensionless wall heat fluxes and total solid mass fraction for case I.

can be related to the irregular, time-dependent nature of solidus front growth. As Fig. 8 illustrates, this growth is alternatingly rapid (rapid decay in $\bar{q}_c^*$) and slow (weak decay in $\bar{q}_c^*$).

For $t^* \lesssim 0.015$, when growth rates are rapid, increases in the average hot wall heat addition ($\bar{q}_h^*$) are smooth. For $t^* \gtrsim 0.015$, however, there are transient random fluctuations in $\bar{q}_h^*$ which persist throughout the numerical simulation. Supporting evidence of such fluctuating behavior has been provided by qualitative experimental observations [7] using bench scale NH_4Cl–H_2O castings. In this investigation, fluctuating behavior is attributed to local growth rate variations or remelting that occurs as a consequence of thermal and solutal fluctuations in the liquid phase. In order for thermal and solutal fluctuations to manifest themselves in remelting (or local growth variations), diffusion coefficients associated with the transport of energy and species must differ ($Le \neq 1$). For the present NH_4Cl–H_2O systems ($Le = 27.8$), energy diffuses more rapidly than species and energy liberated in one region of the casting can cause remelting in surrounding regions of different composition. It has also been observed [7] that remelting occurs only in the absence of steep temperature gradients. The present calculations confirm this observation, as remelting was not predicted in the early stages of solidification and, when predicted, was primarily confined to outer portions of the mushy region. The fluctuations in $\bar{q}_h^*$ (Fig. 8) are therefore attributed to the effect which the formation of liquidus front irregularities has on velocity and temperature fields within the bulk liquid. In contrast, throughout the solidification process, the average solid phase growth rate ($\partial \bar{f}_s/\partial t^*$) remains much smoother, irrespective of localized variations in growth rate or remelting.

Figure 9 illustrates dimensionless hot (q_h^*) and cold (q_c^*) wall heat flux distributions corresponding to the times selected for Figs. 3–7. For each time, heat fluxes at the heated boundary exhibit maxima and minima at the cavity bottom and top, respectively. The smooth

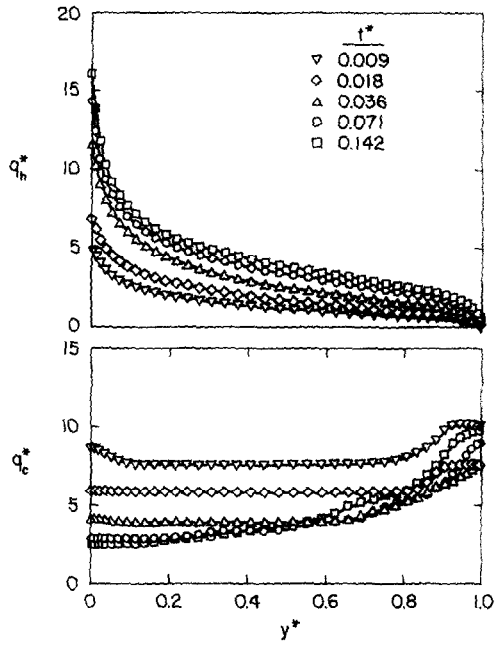

FIG. 9. Dimensionless wall heat flux distributions for case I.

decay in q_h^* with increasing y^* is due to a gradual warming of the fluid as it ascends along the hot boundary. The dimensionless heat flux q_h^*, which can be interpreted as a local Nusselt number defined in terms of the temperature difference $T_0 - T_c$, exhibits trends similar to those for classical single phase cavity problems.

Local cold wall heat extraction rates shown in Fig. 9 suggest that, for early times ($t^* \lesssim 0.018$), heat fluxes are nearly uniform over a large portion ($y^* \lesssim 0.8$) of the chilled boundary. This observation again implies that energy transport during the early stages of solidification is unidirectional and conduction dominated. Increases in q_c^* occurring near the cavity top are attributed to the previously described 'thinning' of the solidus and liquidus fronts. These increases become more pronounced at later stages of the solidification process, indicating a significant deviation from unidirectional, conduction dominated phase change.

3.2. *Insulated sidewall*

Figures 10–14 illustrate solidification behavior for case II at dimensionless times of $t^* = 0.009$, 0.024, 0.214, 0.303, and 0.404, respectively. The graphical presentations correspond to those of case I, except that mushy region streamlines are plotted in increments of $|\psi_{max,s+l}|/5$. Also, since the insulated vertical boundary no longer provides a suitable reference temperature, isotherms presented for case II represent lines of constant $T^* = (T - T_c)/(T_{max} - T_c)$.

Figure 10 illustrates conditions at $t^* = 0.009$

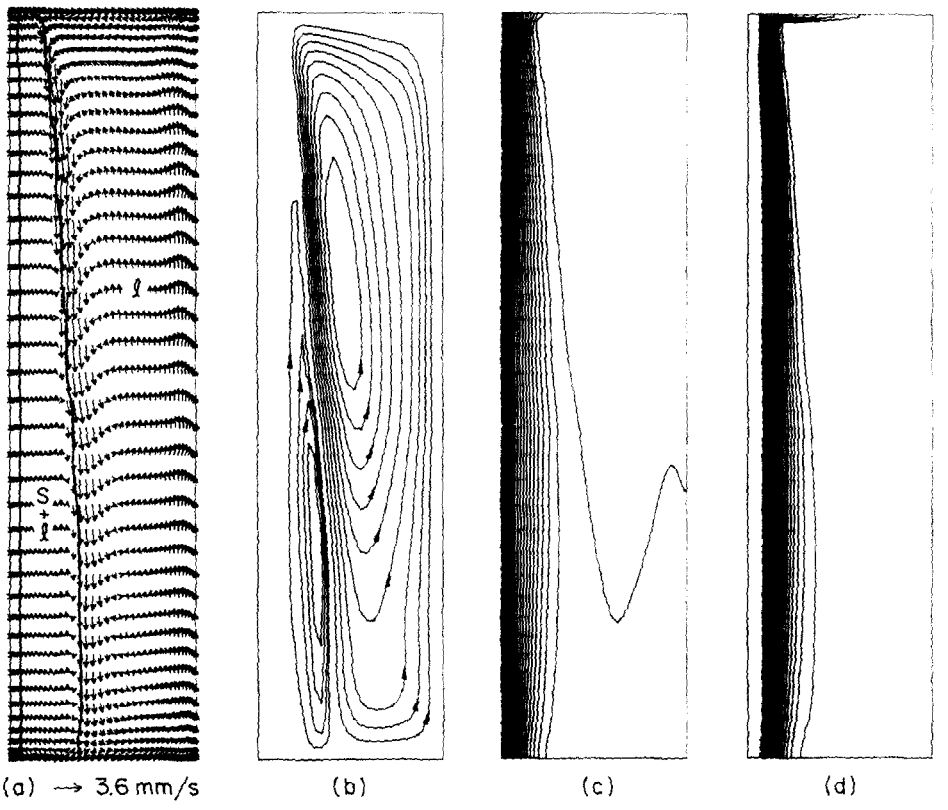

FIG. 10. Solidification behavior at $t^* = 0.009$ for case II: (a) velocity vectors, (b) streamlines ($\psi_{max,l} = 1.07 \times 10^{-2}$, $|\psi_{max,s+l}| = 1.32 \times 10^{-3}$), (c) isotherms ($T_{max} = 310.2$ K), (d) liquid isocomposition lines ($f_{l,min}^* = 0.700$).

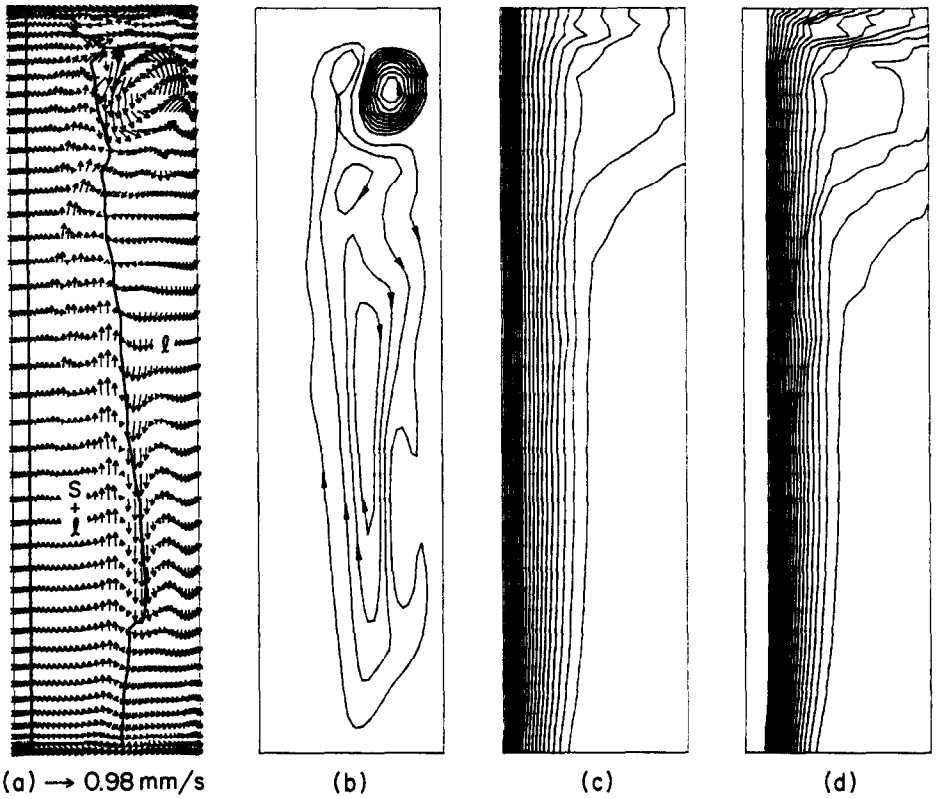

FIG. 11. Solidification behavior at $t^* = 0.024$ for case II: (a) velocity vectors, (b) streamlines ($\psi_{\max,l} = 2.41 \times 10^{-3}$, $|\psi_{\max,s+l}| = 2.33 \times 10^{-3}$), (c) isotherms ($T_{\max} = 305.3$ K), (d) liquid isocomposition lines ($f^{\alpha}_{l,\min} = 0.702$).

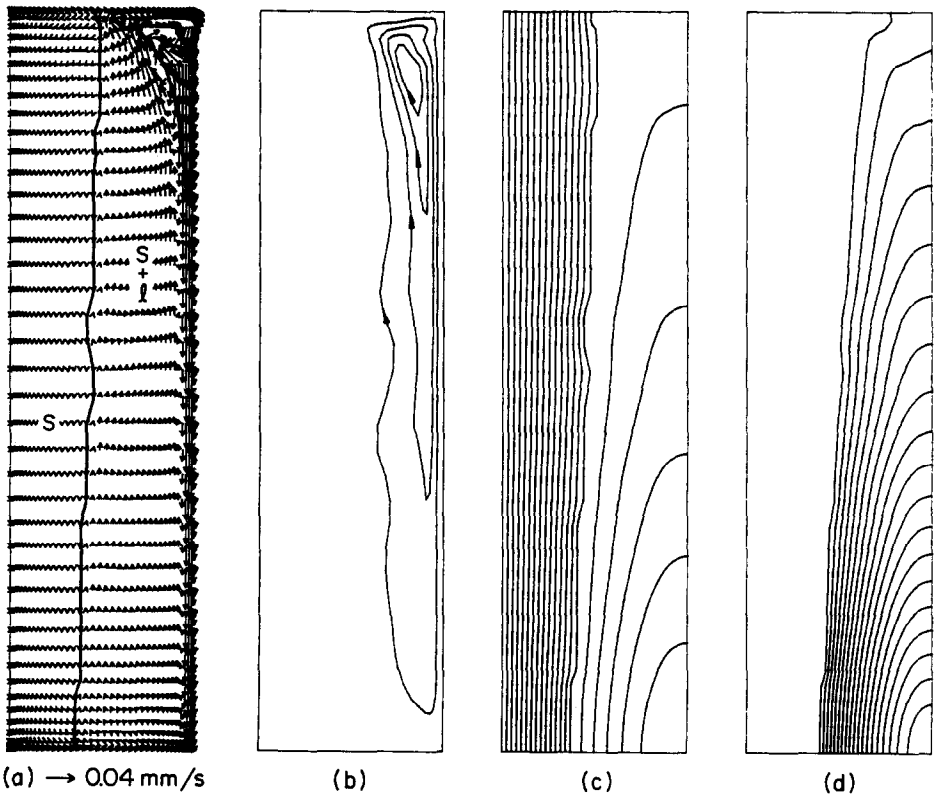

FIG. 12. Solidification behavior at $t^* = 0.214$ for case II: (a) velocity vectors, (b) streamlines ($|\psi_{\max,s+l}| = 1.16 \times 10^{-4}$), (c) isotherms ($T_{\max} = 271.9$ K), (d) liquid isocomposition lines ($f^{\alpha}_{l,\min} = 0.773$).

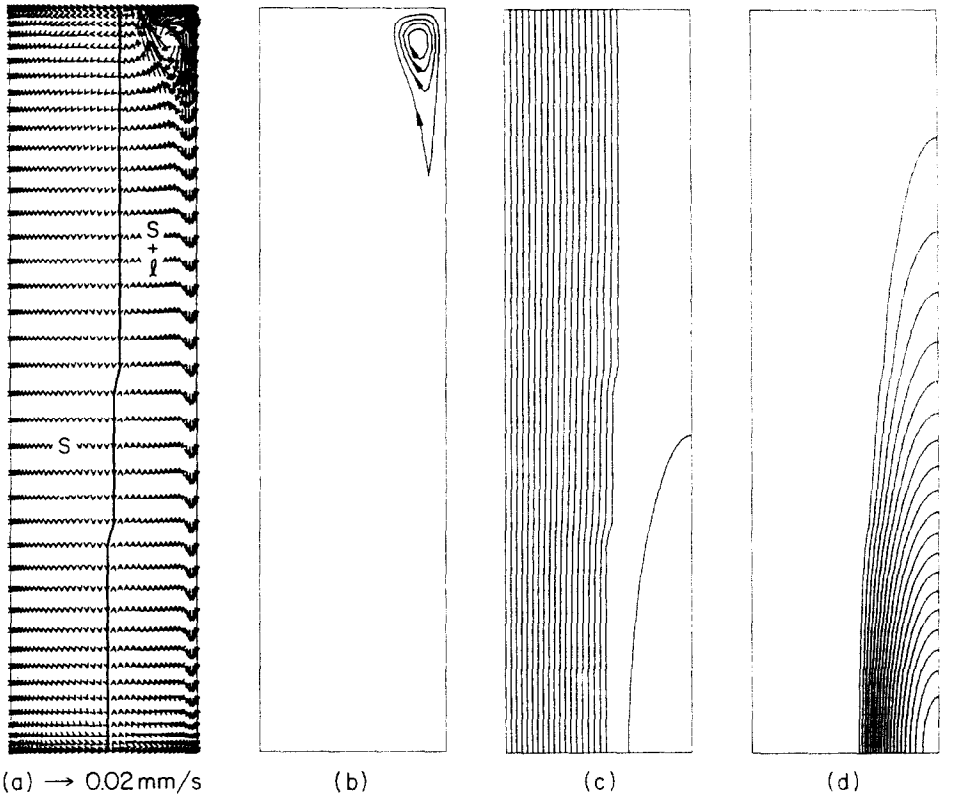

FIG. 13. Solidification behavior at $t^* = 0.303$ for case II: (a) velocity vectors, (b) streamlines ($|\psi_{\max,s+l}| = 5.7 \times 10^{-5}$), (c) isotherms ($T_{\max} = 260.6$ K), (d) liquid isocomposition lines ($f^{\alpha}_{l,\min} = 0.797$).

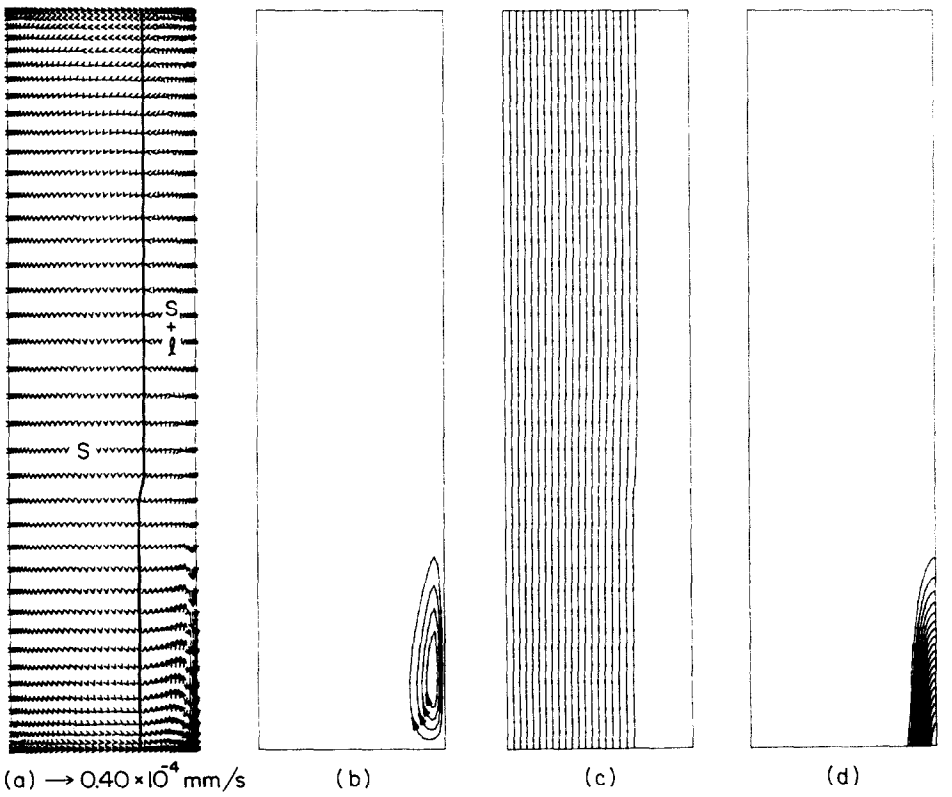

FIG. 14. Solidification behavior at $t^* = 0.404$ for case II: (a) velocity vectors, (b) streamlines ($|\psi_{\max,s+l}| = 3.67 \times 10^{-8}$), (c) isotherms ($T_{\max} = 257.8$ K), (d) liquid isocomposition lines ($f^{\alpha}_{l,\min} = 0.8029$).

($t = 90$ s). While flow in the fluid core is similar to that observed for case I (Fig. 3), the absence of a sustained positive buoyancy force at the vertical insulated boundary significantly weakens the counterclockwise, thermally induced circulation. While somewhat stronger than case I, solutally driven flows are still confined primarily to clockwise circulation within the mushy region. An exception pertains to the local penetration of nearly eutectic composition fluid from the mushy to the liquid region at the cavity top.

Conditions at $t^* = 0.024$ ($t = 240$ s) are illustrated in Fig. 11. Duc to a gradual decay in the initial bulk fluid superheat, mushy region growth is enhanced and thermally induced counterclockwise recirculation is confined to a small cell near the cavity top (Fig. 11(b)). In the absence of a strong downflow outside the liquidus, interdendritic fluids easily penetrate the permeable liquid interface in the top half of the cavity (Fig. 11(a)), establishing a strong clockwise recirculation which, unlike case I, extends significantly beyond the liquidus front (Fig. 11(b)). The downflow of bulk and interdendritic fluids near the liquidus in the central portion of the cavity is attributed to a clockwise, solutally driven recirculation resulting from the water enrichment of interdendritic fluids. Hence, conditions differ sharply from those of case I, which is dominated by counterclockwise, thermally induced bulk fluid recirculation. Through the action of viscous forces, the clockwise, solutally driven recirculation of case II enhances motion within the small, counterclockwise cell near the cavity top and is, in fact, responsible for persistence of the cell well into the solidification process.

As Fig. 11(d) indicates, the outflow of interdendritic fluids from upper portions of the mushy zone establishes a solutally stratified region of water enriched bulk fluids. However, the chilled interdendritic outflow also establishes a thermally unstable condition relative to warmer bulk fluid in lower portions of the cavity (Fig. 11(c)). The S-shaped, horizontal velocity profiles near the cavity bottom (Fig. 11(a)) indicate a stabilizing exchange of warmer and cooler fluid from the cavity bottom and top, respectively.

Irregularities in the liquidus front (Fig. 11(a)) occur primarily near the cavity top and are attributed to the growth rate-reduction which accompanies the water enrichment of bulk fluids. The *thinning* at the cavity bottom is attributed to the inflow of warm bulk fluids which feed the solutally driven flows within the mushy region.

After 2160 s (Fig. 12), the liquidus front has propagated to the insulated vertical boundary and only a small region of highly water enriched bulk fluid remains at the cavity top (Fig. 12(a)). Liquidus temperature depression, which accompanies the water enrichment of this nearly isothermal liquid pool, prohibits nucleation at temperatures well below the liquidus temperature corresponding to the initial composition. The fact that nucleation occurs at the insulated boundary, forming a V-shaped liquidus front, is a clear indication of the influence of local composition variations on solidification behavior.

As Fig. 12(b) illustrates, counterclockwise, thermally driven recirculation no longer exists within the cavity. Solutally driven clockwise recirculation, established by water rejection in the mushy region, again penetrates the liquidus front, entering and leaving the bulk fluid at the cavity top and descending along the vertical insulated boundary. Interdendritic fluid motion is strongest in the outer portions of the mushy region, where permeabilities are large. Contrary to behavior observed in conventional thermally driven phase change systems, the *upflow* of warm interdendritic fluids (Figs. 12(a) and (c)) leads to a *thinning* of the solid layer at the cavity *bottom*.

At $t^* = 0.303$ (Fig. 13), the bulk liquid pool is nearly exhausted. While clockwise recirculation persists (Fig. 13(b)), it is weak ($V_{max} = 0.02$ mm s^{-1}) and concentrated in regions surrounding the liquid pocket at the cavity top. The nearly planar solidus front (Fig. 13(a)) provides further confirmation that conditions are approaching a diffusion dominated state. Isotherms and liquid isocomposition lines depicted in Figs. 13(c) and (d), respectively, indicate that the mushy region is nearly isothermal and that interdendritic fluids are highly water enriched and nearly uniform in composition ($f^{\alpha}_{l,e} - f^{\alpha}_{l,min} = 0.0006$).

Conditions following the total exhaustion of the pure liquid region ($t^* = 0.404$) are illustrated in Fig. 14. Solutally driven mushy region flows are extremely weak ($V_{max} = 0.40 \times 10^{-4}$ mm s^{-1}) and confined to regions of largest permeability at the cavity bottom (Figs. 14(a) and (b)). Temperature gradients are confined to the pure solid region (Fig. 14(c)) and remaining interdendritic fluids are of nearly eutectic water composition (Fig. 14(d)). Beyond $t^* = 0.404$ and proceeding until the cavity is entirely solidified ($t^* = 0.647$), solidification is nearly unidirectional and diffusion dominated.

4. CONCLUSIONS

The capabilities of a newly developed continuum model have been demonstrated through application to solidification of a binary, aqueous solution in a rectangular cavity. Numerical results for aqueous ammonium chloride revealed that fluid motion within the permeable mushy region is characterized by a solutally driven upflow of water enriched, interdendritic fluids. The extent to which these interdendritic fluids penetrate the permeable liquidus interface is strongly influenced by the nature of thermally induced motion in the adjoining liquid core. In the presence of a strong, thermally driven, counter rotating, bulk fluid recirculation, most of the interdendritic flow is confined to recirculation within the mushy region. If the thermally driven, bulk fluid recirculation is weak, however, chilled and water enriched interdendritic fluids penetrate the liquidus, establishing

potentially unstable and double-diffusive conditions within the liquid core. Macroscopic species redistribution, which accompanies this mushy region outflow, significantly affects future phase change behavior contributing to localized growth rate variations, remelting, and the formation of irregular liquidus front morphologies. Combined with the destabilizing influence of exuded interdendritic fluids, macroscopic interfacial irregularities have been shown to induce fluctuations in transport across the bulk liquid core.

Unlike discrete, single constituent phase change, it is difficult to generalize results for binary phase change systems. While nondimensionalization of the conservation equations yields some insight on process complexities, it is unable to collapse all of the pertinent parameters. In addition to depending on individual phase thermophysical properties, solidification depends on microscopic/atomic level characteristics which describe phase interactions and the partitioning of species among coexisting phases. Furthermore, due to complex interactions between thermal and solutal buoyancy forces and their influence on species redistribution, binary system phase change is history dependent and is strongly influenced by externally imposed boundary conditions.

While continuum formulations have received little attention, they provide an attractive alternative to conventional multiple region solutions for problems involving multiconstituent phase change. In fact, for many problems of industrial/scientific significance, which involve complex geometries and boundary conditions, irregular interface morphologies, and/or simultaneous nucleation at mutually exclusive domain locations, continuum formulations may well provide the only viable means of analysis.

Acknowledgement—One of us (W.D.B.) is grateful for support of the Aluminum Company of America under a continuing education grant. Support for a portion of the work has been provided by the National Science Foundation under grant CBT 83-16580.

REFERENCES

1. E. M. Sparrow, S. V Patankar and S. Ramadhyani, Analysis of melting in the presence of natural convection in the melt region, *J. Heat Transfer* **99,** 520–526 (1977).
2. L. S. Yao, Natural convection effects in the continuous casting of a horizontal cylinder, *Int. J. Heat Mass Transfer* **27,** 697–704 (1984).
3. P. G. Kroeger and S. Ostrach, The solution of a two-dimensional freezing problem including convection effects in the liquid region, *Int. J. Heat Mass Transfer* **17,** 1191–1207 (1974).
4. J. Szekely and A. S. Jassal, An experimental and analytical study of the solidification of a binary dendritic system, *Met. Trans. B* **9B,** 389–398 (1978).
5. S. D. Ridder, F. C. Reyes, S. Chakravorty, R. Mehrabian, J. D. Nauman, J. H. Chen and H. J. Klein, Steady state segregation and heat flow in ESR, *Met. Trans. B* **9B,** 415–425 (1978).
6. T. Fujii, D. R. Pourier and M. C. Flemings, Macrosegregation in multicomponent low alloy steel, *Met. Trans. B* **10B,** 331–339 (1979).
7. K. A. Jackson, J. D. Hunt, D. R. Uhlmann and T. P. Seward, III, On the origin of the equiaxed zone in castings, *Trans. Met. Soc. AIME* **236,** 149–158 (1966).
8. R. J. McDonald and J. D. Hunt, Fluid motion through the partially solid regions of a casting and its importance in understanding A type segregation, *Trans. Met. Soc. AIME* **245,** 1993–1997 (1969).
9. R. J. McDonald and J. D. Hunt, Convective fluid motion within the interdendritic liquid of a casting, *Met. Trans.* **1,** 1787–1788 (1970).
10. G. M. Dusinberre, A note on latent heat in digital computer calculations, ASME Paper No. 58-HT-7 (1958).
11. C. L. Jeanfils, J. H. Chen and H. J. Klein, Modeling solidification in an electroslag remelted ingot, *Modeling of Casting and Welding Processes*, pp. 313–332. AIME (1980).
12. A. I. Koler, J. D. Thomas and A. A. Tzavoras, Computations of heat of fusion in a mathematical model for large steel cast shapes, *AFS Cast Metals Res. J.* 156–159 (1973).
13. D. C. Baxter, The fusion times of slabs and cylinders, *J. Heat Transfer* **84,** 317–326 (1962).
14. D. R. Atthey, A finite difference scheme for melting problems, *J. Inst. Math. Applic.* **13,** 353–366 (1974).
15. N. Shamsundar and E. M. Sparrow, Analysis and multidimensional conduction phase change via the enthalpy model, *J. Heat Transfer* **97,** 333–340 (1975).
16. R. N. Hills, D. E. Loper and P. H. Roberts, A thermodynamically consistent model of a mushy zone, *Q. J. Mech. Appl. Math.* **36,** 505–539 (1983).
17. V. C. Prandtl and P. R. Dawson, Application of mixture theory to continued casting. In *Transport Phenomena in Materials Processing* (Edited by M. M. Chen, J. Mazumder and C. L. Tucker), ASME HTD, Vol. 29, pp. 47–54 (1983).
18. W. D. Bennon and F. P. Incropera, A continuum model for momentum, heat and species transport in binary solid–liquid phase change systems—I. Model formulation, *Int. J. Heat Mass Transfer* **30,** 2161–2170 (1987).
19. S. Ostrach, Natural convection in enclosures. In *Advances in Heat Transfer* (Edited by J. P. Hartnett and T. F. Irvine). Academic Press, New York (1972).
20. S. Kakac, W. Aung and R. Viskanta (Editor), *Natural Convection Fundamentals and Applications*. Hemisphere, Washington D.C. (1985).
21. R. H. Marshall, Natural convection effect in rectangular enclosures containing a phase change material. In *Thermal Storage and Heat Transfer in Solar Energy Systems* (Edited by F. Kreith, R. Boehm, J. Mitchell and R. Bannerot). ASME, New York (1978).
22. R. H. Henze and J. A. C. Humphrey, Enhanced heat conduction in phase-change energy storage devices, *Int. J. Heat Mass Transfer* **24,** 459 (1981).
23. S. Ostrach, Natural convection with combined driving forces, *PhysicoChem. Hydrodyn.* **1,** 233–247 (1980).
24. S. R. Coriell, M. R. Cordes, W. J. Boettinger and R. F. Sekerka, Convective and interfacial instabilities during unidirectional solidification of a binary alloy, *J. Crystal Growth* **49,** 13–28 (1980).
25. R. A. Brown, C. J. Chang and P. M. Adornato, Finite element analysis of directional solidification of dilute and concentrated binary alloys, *Modeling of Casting and Welding Processes*. AIME (1984).
26. S. Asai and I. Muchi, Theoretical analysis and model experiments on the formation mechanism of channel-type segregation, *Trans. ISIJ* **18,** 90–98 (1978).
27. R. B. Bird, W. E. Stewart and E. N. Lightfoot, *Transport Phenomena*. Wiley, New York (1960).
28. S. V. Patankar, A calculation procedure for two-dimensional elliptic situations, *Numer. Heat Transfer* **4,** 409–425 (1981).
29. G. deVahl Davis, Natural convection of air in a square cavity: a benchmark numerical solution, *Int. J. Numer. Meth. Fluids* **3,** 249–264 (1983).

30. S. Witzke, J. P. Riquet and F. Durand, Diffusion field ahead of growing columnar front: discussion of the columnar-equiaxed transition, *Acta Metall.* **29**, 365–375 (1981).
31. *International Critical Tables of Numerical Data, Physics, Chemistry, and Technology*, Vols 3 and 4 (1928).
32. J. S. Turner, *Buoyancy Effects in Fluids*. Cambridge University Press, Cambridge (1973).

UN MODELE CONTINU POUR LA QUANTITE DE MOUVEMENT, LA CONVECTION DE CHALEUR ET DE MASSE DANS LES SYSTEMES A CHANGEMENT DE PHASE SOLIDE–LIQUIDE—II. APPLICATION A LA SOLIDIFICATION DANS UNE CAVITE RECTANGULAIRE

Résumé—Un modèle nouveau est utilisé avec un schéma bien établi à volumes de contrôle et différences finies pour étudier la solidification d'une solution aqueuse de chlorure d'ammonium dans une cavité rectangulaire. Le transfert advectif des fluides interdendritiques à travers l'interface perméable du liquidus est identifié comme le mécanisme primaire d'une redistribution macroscopique des espèces. L'étendue de cette pénétration est gouvernée par les intensités relatives des écoulements de la région mixte et des écoulements thermiquement conduits dans la masse liquide. Des conditions instables et doublement diffusifs qui accompagnent la décharge des fluides interdendritiques vers le coeur liquide résultent des variations locales de vitesse de croissance, de la refusion et du comportement fluctuant du transport global de fluide.

EIN MODELL FÜR IMPULS-, WÄRME- UND STOFFTRANSPORT IN BINÄREN FEST-FLÜSSIG-PHASENWECHSELSYSTEMEN—II. ANWENDUNG AUF DIE ERSTARRUNG IN EINEM RECHTECKIGEN HOHLRAUM

Zusammenfassung—Die Verfestigung einer binären, wässrigen Ammonium-Chlorid-Lösung in einem rechteckigen Hohlraum wurde mit Hilfe eines jüngst entwickelten Kontinuum-Modells untersucht. Die Lösung erfolgte mit einem wohlerprobten Finite-Differenzen-Verfahren. Der advektive Transport von interdentritischem, mit Wasser angereichertem Fluid wurde als primärer Mechanismus für die makroskopische Stoffverteilung erkannt. Das Ausmaß dieser Eindringung wird durch die relative Stärke der konzentrationsgetriebenen Strömung in der noch weichen Zone und der thermisch getriebenen Strömung im Kern bestimmt. Instabile und doppel-diffusive Bedingungen, die das Endringen des interdendritischen Fluids in den flüssigen Kern begleiten, wurden als Verursacher von lokalen Unterschieden der Wachstumsrate, von Wiederschmelzungen und von veränderlichem Transportverhalten im Flüssigkeitskern aufgezeigt.

ФЕНОМЕНОЛОГИЧЕСКИЕ УРАВНЕНИЯ ПЕРЕНОСА КОЛИЧЕСТВА ДВИЖЕНИЯ, ТЕПЛА И МАССЫ В БИНАРНЫХ СИСТЕМАХ ТВЕРДОЕ ТЕЛО–ЖИДКОСТЬ ПРИ ФАЗОВЫХ ИЗМЕНЕНИЯХ—II. ПРИМЕНЕНИЕ ДЛЯ СЛУЧАЯ ЗАТВЕРДЕВАНИЯ В ПРЯМОУГОЛЬНОЙ ПОЛОСТИ

Аннотация—Для исследования затвердевания бинарного раствора водного хлористого аммиака в прямоугольной полости используется недавно разработанная модель процессов переноса совместно с ее численной реализацией. В качестве основного механизма перераспределения макроскопических количеств вещества рассматривается перенос в воде взаимнодендритовых жидкостей поперек проницаемой поверхности раздела ликвидуса. Величина этого проникновения зависит от относительных значений растворимости и тепловых потоков в объеме жидкости. Показано, что условия неустановившейся и взаимной диффузии, которые сопровождают расход внутридендритовых жидкостей в ядро потока жидкости, приводят к локальным изменениям скорости роста, повторному плавлению и к флуктуациям в процессах переноса в объеме жидкости.